A&A 662, A115 (2022)
https://doi.org/10.1051/0004-6361/202243348

Astronomy & Astrophysics

The ionizing properties of two bright Lyα emitters in the Bremer Deep Field reionized bubble at $z = 7$

M. Castellano[1], L. Pentericci[1], G. Cupani[2], E. Curtis-Lake[3], E. Vanzella[4], R. Amorín[5,6], D. Belfiori[1], A. Calabrò[1], S. Carniani[7], S. Charlot[8], J. Chevallard[9], P. Dayal[10], M. Dickinson[11], A. Ferrara[7], A. Fontana[1], E. Giallongo[1], A. Hutter[10], E. Merlin[1], D. Paris[1], and P. Santini[1]

[1] INAF – OAR, Via Frascati 33, 00078 Monte Porzio Catone (Roma), Italy
e-mail: marco.castellano@inaf.it
[2] INAF – Osservatorio Astronomico di Trieste, Via G. B. Tiepolo 11, 34143 Trieste, Italy
[3] Centre for Astrophysics Research, Department of Physics, Astronomy and Mathematics, University of Hertfordshire, Hatfield AL10 9AB, UK
[4] INAF – OAS, Osservatorio di Astrofisica e Scienza dello Spazio di Bologna, Via Gobetti 93/3, 40129 Bologna, Italy
[5] Departamento de Astronomía, Universidad de La Serena, Av. Juan Cisternas 1200 Norte, La Serena, Chile
[6] Instituto de Investigación Multidisciplinar en Ciencia y Tecnología, Universidad de La Serena, Raúl Bitrán 1305, La Serena, Chile
[7] Scuola Normale Superiore, Piazza dei Cavalieri 7, 56126 Pisa, Italy
[8] Sorbonne Université, CNRS, UMR7095, Institut d'Astrophysique de Paris, 75014 Paris, France
[9] Astrophysics, The Denys Wilkinson Building, University of Oxford, Keble Road, Oxford OX1 3RH, UK
[10] Kapteyn Astronomical Institute, University of Groningen, PO Box 800, 9700 AV Groningen, The Netherlands
[11] NSF's NOIRLab, Tucson, AZ 85719, USA

Received 17 February 2022 / Accepted 6 May 2022

ABSTRACT

Aims. We investigate the ionizing properties of the pair of bright Lyα emitting galaxies BDF521 and BDF2195 at $z = 7.012$ in order to constrain their contribution to the formation of the Bremer Deep Field (BDF) 'reionized bubble' in which they have been shown to reside.

Methods. We obtain constraints on four UV emission lines (the CIVλ1548 doublet, HeIIλ1640, the OIII]λ1660 doublet, and the CIII]λ1909 doublet) from deep VLT X-shooter observations and compare them to those available for other high-redshift objects, and to models with mixed stellar and active galactic nucleus (AGN) emission. We use this spectroscopic information, together with the photometry available in the field, to constrain the physical properties of the two objects using the spectro-photometric fitting code BEAGLE.

Results. We do not detect any significant emission at the expected position of the UV lines, with 3σ upper limits of equivalent width (EW) $\lesssim$2–7 Å rest-frame. We find that the two objects have a lower CIII] emission than expected on the basis of the correlation between the Lyα and CIII] EWs. The EW limits on CIV and HeII emission exclude pure AGN templates at $\sim$2–3σ significance, and only models with a $\lesssim$40% AGN contribution are compatible with the observations. The two objects are found to be relatively young ($\sim$20–30 Myrs) and metal-poor ($\lesssim 0.3\,Z_\odot$), with stellar masses of a few $10^9\,M_\odot$. Their production rate of hydrogen ionizing photons per intrinsic UV luminosity is $\log(\xi^*_{\rm ion}/{\rm Hz\,erg^{-1}}) = 25.02$–$25.26$, consistent with values typically found in high-redshift galaxies, but more than twice lower than values measured in $z > 7$ galaxies with strong CIII] and/or optical line emission ($\simeq$25.6–25.7).

Conclusions. The two BDF emitters show no evidence of higher-than-average ionizing capabilities and are not capable of reionizing their surroundings by their own means, under realistic assumptions of the escape fraction of ionizing photons. Therefore, a dominant contribution to the formation of the reionized bubble must have been provided by fainter companion galaxies. The capabilities of the *James Webb* Space Telescope will be needed for spectroscopic confirmation of these objects.

Key words. galaxies: evolution – galaxies: high-redshift – dark ages, reionization, first stars

1. Introduction

The epoch of reionization (EoR) marked a major phase transition of the Universe, during which the intergalactic medium (IGM) became transparent to UV photons. Determining the physical processes involved in the reionization process, its timeline, and topology represents the latest frontier in observational cosmology (Dayal & Ferrara 2018).

The first indication of an increased neutral hydrogen fraction ($\chi_{\rm HI}$) in the IGM at $z \gtrsim 6$ was obtained through observations of the Gunn–Peterson effect in distant quasars (Fan et al. 2002). However, a substantial step in our knowledge of the reionization timeline has been made possible only by constraints on the redshift evolution of the fraction of Lyman-break galaxies (LBGs) that have an appreciable Lyα emission line (e.g., Malhotra & Rhoads 2006; Stark et al. 2010; Fontana et al. 2010). In fact, the neutral hydrogen in the IGM scatters Lyα photons out of the line-of-sight, such that a lower line visibility indicates a higher IGM neutral fraction if the properties of the interstellar medium (ISM) remain unchanged (e.g., Dayal et al. 2011; Dijkstra 2019). A decrease in the Lyα fraction at $z \gtrsim 6$ has been confirmed by many independent analyses, and this has been interpreted as an indication of an increasing neutral hydrogen fraction in the IGM (e.g., Pentericci et al. 2011, 2018;

Schenker et al. 2012; Ono et al. 2012; Mason et al. 2018, 2019). Together with measurements of the cosmic microwave background Thomson optical depth (Planck Collaboration 2020), of the clustering of Lyα-emitters (LAEs, Hutter et al. 2015; Sobacchi & Mesinger 2015), and with measurements of ionized regions around the most distant quasi-stellar objects (QSOs) (e.g., Bañados et al. 2018), the available observations point to a scenario in which the Universe was still substantially neutral at $z \sim 10$ ($\chi_{\rm HI} \gtrsim 90\%$) and was rapidly reionized in ~ 500 Myr, ending the EoR at $z \sim 5.5$–6 (e.g., Mitra et al. 2015, 2018; Greig & Mesinger 2017; Hutter et al. 2021). Star-forming galaxies are currently considered to be the most likely sources of reionizing photons (e.g., Robertson et al. 2015; Bouwens et al. 2015a; Dayal et al. 2020; Endsley et al. 2021b; Romanello et al. 2021), although our poor knowledge of galaxy physical properties does not allow us to rule out that active galactic nuclei (AGN) also contributed (Finkelstein et al. 2019; Giallongo et al. 2015).

The rate of ionizing photons escaping into the IGM from a given population is $\dot{N} = \rho_{\rm UV} \xi^*_{\rm ion} f_{\rm esc}$, where $\rho_{\rm UV}$ is the total, dust-corrected UV luminosity density at 1500 Å, $\xi^*_{\rm ion}$ is the ionizing photon production efficiency per unit UV luminosity, and $f_{\rm esc}$ is the fraction of ionizing photons leaked into the surrounding environment. Currently, the UV luminosity density from star-forming galaxies is well constrained by measurements of their UV luminosity function (LF) at $z > 6$ down to $L < L^*$ (e.g., Bouwens et al. 2015b; Livermore et al. 2017; Ishigaki et al. 2018; Yue et al. 2018; Oesch et al. 2018). However, the escape fraction of ionizing photons can only be directly constrained at $z \lesssim 3$–4 and on average is quite modest in LBGs with values lower than 5–10% (Boutsia et al. 2011; Marchi et al. 2017; Grazian et al. 2017; Steidel et al. 2018; Pahl et al. 2021). Only in a few rare objects does it reach values of $f_{\rm esc} \gtrsim 50\%$ (de Barros et al. 2016; Vanzella et al. 2016, 2018; Naidu et al. 2017; Izotov et al. 2018a,b; Flury et al. 2022). At present, no real constraints exist on a possible increase in the $f_{\rm esc}$ with redshift, and we can only make assumptions as to its value in the EoR.

The ionizing efficiency $\xi^*_{\rm ion}$ can be directly obtained by measuring, at the same time, the non-ionizing UV continuum and the Balmer emission lines, the latter yielding the emission rate of ionizing photons (e.g., Shivaei et al. 2018), or from the equivalent width (EW) of the [OIII]λ4959, 5007 doublet (Chevallard et al. 2018; Tang et al. 2019). At higher redshifts where optical emission lines are not directly observable through spectroscopy, constraints on $\xi^*_{\rm ion}$ were derived by the analysis of the rest-frame UV colours (e.g., Duncan & Conselice 2015) or from the contamination from strong emission lines to the mid-IR colours, with a typical $\log(\xi^*_{\rm ion}/{\rm Hz\,erg^{-1}}) \simeq 25.3$ at $z \sim 4$–5 (Bouwens et al. 2016; Lam et al. 2019) found, with indication of higher ionizing efficiencies in LAEs (Harikane et al. 2018; Sobral & Matthee 2019) and strong [OIII]λ4959, 5007 emitters (Tang et al. 2019).

For galaxies in the EoR, constraints on the ionizing capabilities can be derived using UV emission lines. These, however, are extremely faint and have been detected only in a handful of objects (e.g., Stark et al. 2015a,b; Laporte et al. 2017; Mainali et al. 2018; Hutchison et al. 2019; Topping et al. 2021).

Such features might be associated with AGN or metal-poor stellar populations (Gutkin et al. 2016; Feltre et al. 2016; Nakajima et al. 2018b), as also shown at lower redshifts (e.g., Amorín et al. 2017; Calabrò et al. 2017; Nakajima et al. 2018a). The spectro-photometric analysis of a CIV emitter at $z = 7.045$ allowed Stark et al. (2015b) to estimate an ionizing efficiency of $\log(\xi^*_{\rm ion}/{\rm Hz\,erg^{-1}}) \simeq 25.68$, much higher than the typical value measured at lower redshifts and comparable to values measured in rare, extreme emission line galaxies at $z \sim 3$–4 (Nakajima et al. 2016). Similarly, spectroscopically confirmed $z > 7$ galaxies with mid-IR colours that suggest intense Hβ+[OIII] emission show a $\log(\xi^*_{\rm ion}/{\rm Hz\,erg^{-1}}) \gtrsim 25.5$ (Stark et al. 2017; Endsley et al. 2021a). These results point to an increased fraction of galaxies with a high ionizing efficiency in the EoR.

A promising way to shed light on the sources of reionization is to investigate regions where this process is more advanced, and observations point to the presence of 'reionized bubbles' (Castellano et al. 2016a; Higuchi et al. 2019; Tilvi et al. 2020; Jung et al. 2021; Leonova et al. 2021; Endsley & Stark 2022). The analysis of the Lyα fraction in independent lines-of-sight suggests that reionization was a spatially inhomogeneous process (Treu et al. 2012; Pentericci et al. 2014). A detailed spectroscopic investigation of the Bremer Deep Field (BDF) (Lehnert & Bremer 2003; Castellano et al. 2010) led to the first discovery of a likely reionized 'bubble' at $z \sim 7$ (Castellano et al. 2016a, hereafter C16). The BDF hosts three bright ($L \sim L^*$) Lyα emitting galaxies with EW > 50 Å (Vanzella et al. 2011; Castellano et al. 2018, hereafter V11 and C18), and the density of $z \simeq 7$ faint LBGs in this area is $\gtrsim$3–4 times higher than the average (C16). Two of the Lyα emitting galaxies (BDF521 and BDF2195) have exactly the same redshift and are at a projected physical separation of only 91.3 kpc, the third one, BDF3299, being at a projected distance of 1.9 proper Mpc.

The high number density of LBGs in the BDF region is consistent with the clustered faint galaxies being key contributors to the local reionization history (C16, Rodríguez Espinosa et al. 2021), as expected in 'inside-out' reionization scenarios (Choudhury et al. 2009; Dayal et al. 2009; Trebitsch et al. 2021). However, significant uncertainties remain due to the lack of Lyα detections in the faint companion galaxies, despite significant observational efforts (C18). Lacking a spectroscopic confirmation of the faint LBGs in the field, it is fundamental to fully constrain the physical properties of the bright emitters and assess whether they can create the reionized region, possibly due to hard-ionizing stellar populations or AGN.

In this paper we analyse deep Very Large Telescope (VLT) X-shooter observations of the BDF521 and BDF2195 pair to put constraints on the ionizing budget of the two emitters from UV rest-frame metal emission lines, and to ascertain whether these $L \simeq L^*$ galaxies play a major role in the creation of the BDF bubble.

The paper is organized as follows: in Sect. 2 we present the observations and data reduction, and in Sect. 3 we discuss the constraints on emission lines and compare the BDF galaxies to other high-redshift sources. We place constraints on the contribution from AGN in Sect. 4, and then quantify their physical properties and their contribution to the creation of the BDF bubble in Sect. 5. The results are summarized in Sect. 6.

Throughout the paper, we adopt AB magnitudes (Oke & Gunn 1983), a solar metallicity $Z_\odot = 0.02$, and a Λ-cold dark matter concordance model ($H_0 = 70\,{\rm km\,s^{-1}\,Mpc^{-1}}$, $\Omega_{\rm M} = 0.3$, and $\Omega_\Lambda = 0.7$).

2. The X-shooter observations

The BDF521 and BDF2195 pair was observed by X-shooter in nodding mode with 11×0.9 arcsec slits, and 900 and 865 s per single exposure in the near-infrared (NIR) and visible (VIS) arms, respectively. Observations were acquired between 26 September 2019 and 8 June 2021. The total observing time was

15 h for BDF521 and 12 h for BDF2195, corresponding to on-target exposure times of 12.0 (11.5) and 9.5 (9.1) h in the NIR (VIS).

Science frames were reduced with the official X-shooter pipeline (Modigliani et al. 2010), v. 3.3.5, using the associated raw calibrations from the ESO archive. Sky subtraction was performed using the X-shooter nodding strategy, combining frames acquired at two different positions in the sky for each OB execution. A fixed boxcar window was used to extract the target on the rectified 2D spectra, to ensure that the target was correctly localized along the slit (`extractmethod=LOCALIZATION` and `localizemethod=MANUAL` in pipeline recipe `xsh_scired_slit_nod`). The position of the window (with respect to the slit centre) and its half height (in arcsec) were fine-tuned for the two targets independently, based on the position of the Lyα line, which is well detected in the 2D VIS median stacked spectra (and visible in each single OB); we used `localize-slit-position=-1.0`, `localize-slit-hheight=0.5` for BDF521 and `localize--slit-position=-3.2`, `localize-slit-hheight=0.6` for BDF2195 in pipeline recipe `xsh_scired_slit_nod`.

The 1D extracted spectra, one for each X-shooter arm and OB execution, were corrected to the barycentric reference frame in vacuum and combined with the data analysis package AstroCook (Cupani et al. 2020). The combined spectra were rebinned to 18 km s^{-1} in the NIR arm and to 11 km s^{-1} in the VIS arm, roughly corresponding to 3 pixels per resolution element, given the nominal full width at half maximum (FWHM) resolution of the instrument in the three arms for the adopted slit. Undersampled spectra with larger spectral bins (54 km s^{-1} in the NIR arm, 33 km s^{-1} in the VIS arm) were also produced to facilitate the identification of spectral features by visual inspection.

While the slits are not designed to include the total flux from the observed objects, following Lemaux et al. (2009), we expect slit losses to be small (~10–15%) on the basis of the slit dimension, the compact size of the sources (~0.15″), and the median seeing (~0.8″) of the X-shooter observations. In order to quantitatively assess the significance of potential slit losses, we smoothed the *Hubble* Space Telescope *F*125*W* image (C16) of the objects to the seeing of the spectroscopic observations and measured the fraction of the total flux observed within the slit size. We found corrections of ~10% that are uncertain, however, due to effects of light contamination from other objects and the local background subtraction of the images. Therefore, we decided not to apply correction factors in the following.

3. Constraints on UV rest-frame line emission

At the Lyα redshift estimated from FORS2 (z = 7.008, C18), the VIS arm of the instrument covers the Lyα line, while the NIR arm covers the range of the CIV doublet (1548 Å–1550 Å), HeIIλ1640, the OIII] doublet (1661 Å–1666 Å), and the CIII] doublet (1907 Å–1909 Å). First, we visually inspected the spectra to localize the Lyα emission and obtain a precise positioning of the object within the slit.

3.1. Lyα emission

We detected Lyα line emission for both objects: the flux-weighted mean wavelength of the line corresponds to z = 7.0121 for BDF521 and z = 7.0124 for BDF2195. These redshifts are slightly higher than previously estimated from the peak of the Lyα emission in FORS2 spectra (z = 7.008) but do confirm that the objects are approximately at the same redshift and, given the close separation on the sky (91.3 kpc, C18), are likely physically connected. We use these new estimates in the present analysis. The total Lyα fluxes are 12.8 ± 1.0 for BDF521 and 21.8 ± 1.1 × 10^{-18} erg s^{-1} cm^{-2} for BDF2195. The widths in velocity space and the EWs of the lines are consistent with previous analyses. We find EW(Lyα) = 60 ± 5 Å, FWHM(Lyα) = 263 ± 5 km s^{-1} for BDF521, and EW(Lyα) = 62 ± 3 Å, FWHM(Lyα) = 250 ± 3 km s^{-1} for BDF2195. The continuum flux was estimated on the basis of the available photometry (C16). The FWHM was measured with a Gaussian fit and corrected for the effect of instrumental resolution. Uncertainties were computed following Lenz & Ayres (1992). The VIS arm also covers the expected range of the NVλ 1240 doublet, but in a noisy, low efficiency region of the spectrum that does not allow us to improve upon the limits previously obtained with FORS2 (C18).

Table 1. 3σ upper limits on the observed fluxes and the rest-frame EW of the UV emission lines of BDF521 and BDF2195.

Line	BDF521		BDF2195	
	Flux 10^{-18} erg s^{-1} cm^{-2}	EW Å	Flux 10^{-18} erg s^{-1} cm^{-2}	EW Å
CIV1548.20	<1.40	<7.18	<1.93	<5.77
CIV1550.78	<1.42	<7.30	<1.79	<5.58
HeII1640.42	<1.47	<5.86	<1.81	<4.34
OIII1660.81	<1.58	<6.49	<1.80	<3.98
OIII1666.15	<1.58	<5.96	<2.02	<4.64
CIII1906.68	<1.35	<1.96	<1.81	<1.85
CIII1908.73	<1.45	<2.40	<1.87	<2.16

3.2. Limits on UV metal lines

We inspected both 2D and 1D spectra to assess the presence of metal UV emission lines. We detected no continuum emission and found no significant features within 500 km s^{-1} of the position expected on the basis of the Lyα redshift. In general, no evident line emission is found elsewhere at the objects' positions in the NIR arm spectra. Considering the Lyα velocity offset range expected for bright z ~ 7 galaxies (e.g., Maiolino et al. 2015; Mason et al. 2018), we estimated upper limits for the flux of all lines from the average flux uncertainty in a moving window of 100 km s^{-1} rest-frame across the range between −500 km s^{-1} and 0 km s^{-1} from the Lyα redshift while masking sky line residuals. We derive corresponding EW limits after estimating the continuum flux at each position on the basis of the observed photometry (C16). Namely, we follow the standard assumption of approximating the UV continuum as a power law $F_\lambda \propto \lambda^\beta$ whose slope β can be measured from a regression across the observed bands (e.g., Castellano et al. 2012). The measured slopes are $\beta = -2.25 \pm 0.25$ for BDF521 and $\beta = -1.66 \pm 0.16$ for BDF2195. We find rest-frame EW limits $\lesssim$2–7 Å at 3σ (Table 1). The limit on HeII emission for BDF521 is consistent with the estimate obtained by Cai et al. (2015) from narrow-band HST photometry. The spectra at the expected positions of the relevant lines are shown in Figs. A.1 and A.2.

3.3. Comparison with other high-redshift sources

In the last few years, several groups have actively searched for UV emission lines in the most distant galaxies, as valuable

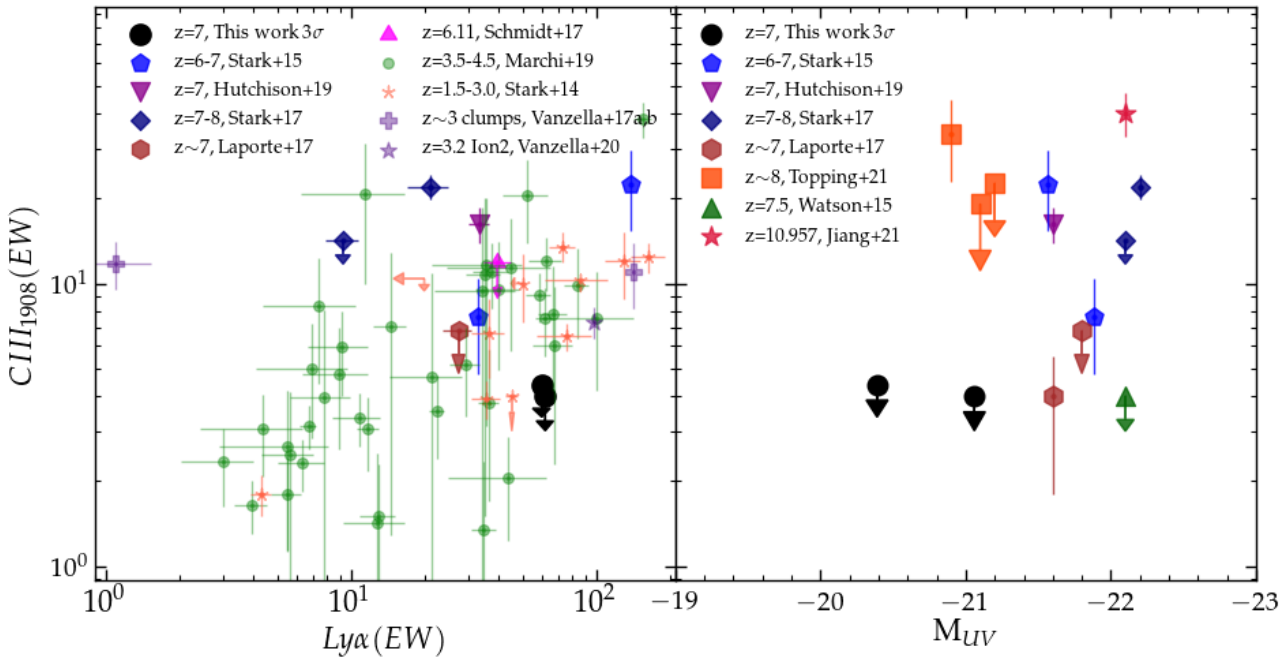

Fig. 1. Position of BDF521 and BDF2195 on the CIII](EW) vs. Lyα(EW) plane (*left panel*), and on the CIII](EW) vs. $M_{\rm UV}$ plane (*right panel*), compared to $z \gtrsim 6$ objects from the literature: Stark et al. (2015a), Watson et al. (2015), Stark et al. (2017), Laporte et al. (2017), Schmidt et al. (2017), Hutchison et al. (2019), Jiang et al. (2021), and Topping et al. (2021). In the left panel we also show objects at $z \sim 1.5$–3 from Stark et al. (2014), the CIII] emitters at $z = 3.5$–4.5 from the VANDELS survey (Marchi et al. 2019), the Lyman-continuum leaker Ion2 ($z = 3.2$, Vanzella et al. 2020), and the ultra-faint star-forming clumps at $z \sim 3$ from Vanzella et al. (2017a,b). All upper limits are at 3σ. See the legend for symbols and colours.

diagnostics of the underlying radiation field (e.g., Mainali et al. 2018; Stark et al. 2017; Laporte et al. 2017; Endsley et al. 2021a) and in some case as redshift indicators, in the absence of Lyα (Jiang et al. 2021). The second most common line, after Lyα, is the CIII] doublet, which has been detected in several of the most distant galaxies, including the most distant spectroscopically confirmed galaxy GN-z11 at $z = 10.957$ (Oesch et al. 2016; Jiang et al. 2021). At $z \sim 3$–4, a strong correlation between the Lyα and CIII] strength has been found by several authors (Stark et al. 2014; Marchi et al. 2019), although in other cases a large scatter between the quantities was also observed (Le Fèvre et al. 2019; Rigby et al. 2015; Llerena et al. 2022; Schmidt et al. 2021). Confirmed (Vanzella et al. 2020) or suspected $z \sim 3$ Lyman-continuum leakers (Vanzella et al. 2017a,b) either fall on the expected relation or rather show significant CIII] emission and suppressed Lyα emission.

It is unclear whether the relation holds at $z \gtrsim 6$, where only a few detections are available. The reported detections we show in the left panel of Fig. 1 seem to agree with the lower-redshift behaviour, while our two BDF emitters do not follow the expected trend. Indeed, the galaxies have rather large Lyα EW, and we would expect solid detections of the CIII] doublet at $>5\sigma$ from the average of lower redshift relations, although the BDF objects are consistent with the lower envelope of the measured distributions. As shown in the right panel of Fig. 1, all high-redshift objects with a secure CIII] detection are bright, $L \gtrsim L*$ LBGs (i.e., $M_{\rm UV} \lesssim -20.5$, e.g., Harikane et al. 2022), and in most cases, significantly brighter than the BDF emitters.

Llerena et al. (2022) find that strong CIII] emitters at $z \sim 3$ have strong radiation fields and a low stellar metallicity, but their gas is already partially enriched with C/O abundances in the range 35%–150% solar. In this respect, the lack of strong CIII] emission can be explained either by an extremely low C abundance in the gas phase, and/or by the objects being in a less active star-formation phase (Berg et al. 2019). In the case of the BDF galaxies, a low metallicity is likely the main factor affecting the low CIII] emission, given the high Lyα EW, suggesting active star formation. A low metallicity is also consistent with the lack of CII158 µm detection in BDF521 (Maiolino et al. 2015). A strong starburst phase that photodissociates the molecular clouds could also lower CII158 µm emission (Pallottini et al. 2019), but UV CIII] emission should be enhanced in such a situation if C is abundant in the ionized gas.

In Fig. 2 we compare the limits we obtained for the CIV emission on the two BDF galaxies to previous studies. In the EoR there are only two galaxies where a convincing CIV emission is detected: the gravitationally lensed low-mass galaxies RXC J2248.7−4431-ID3 ($z = 6.11$, Mainali et al. 2017), and A1703-zd6 ($z = 7.045$, Stark et al. 2015b). Several attempts to detect this line in small samples of galaxies at $z = 6$–10 have failed to report detections (Laporte et al. 2017; Mainali et al. 2018; Shibuya et al. 2018), with typical EW limits around 3–10 Å, similar to the BDF galaxies. Although an AGN contribution to the Lyα flux cannot be completely ruled out, the CIV EWs and $f_{\rm CIV}/f_{\rm Ly\alpha}$ ratios for the two BDF galaxies are low compared to most known Type II AGN at intermediate redshift (Alexandroff et al. 2013), and much lower than those for the two $z > 6$ LBGs with CIV detections (left panel of Fig. 2). These results are consistent with the analysis of the Lyα/NV ratio from FORS2 spectroscopy (C18). The two BDF galaxies have Lyα/NV $\gtrsim 8$–10, which is higher than the values measured in suspected AGN at $z \gtrsim 7$ (e.g., Tilvi et al. 2016; Laporte et al. 2017; Mainali et al. 2018), albeit still consistent with values observed in AGN at lower redshifts (Humphrey et al. 2008; Hainline et al. 2011).

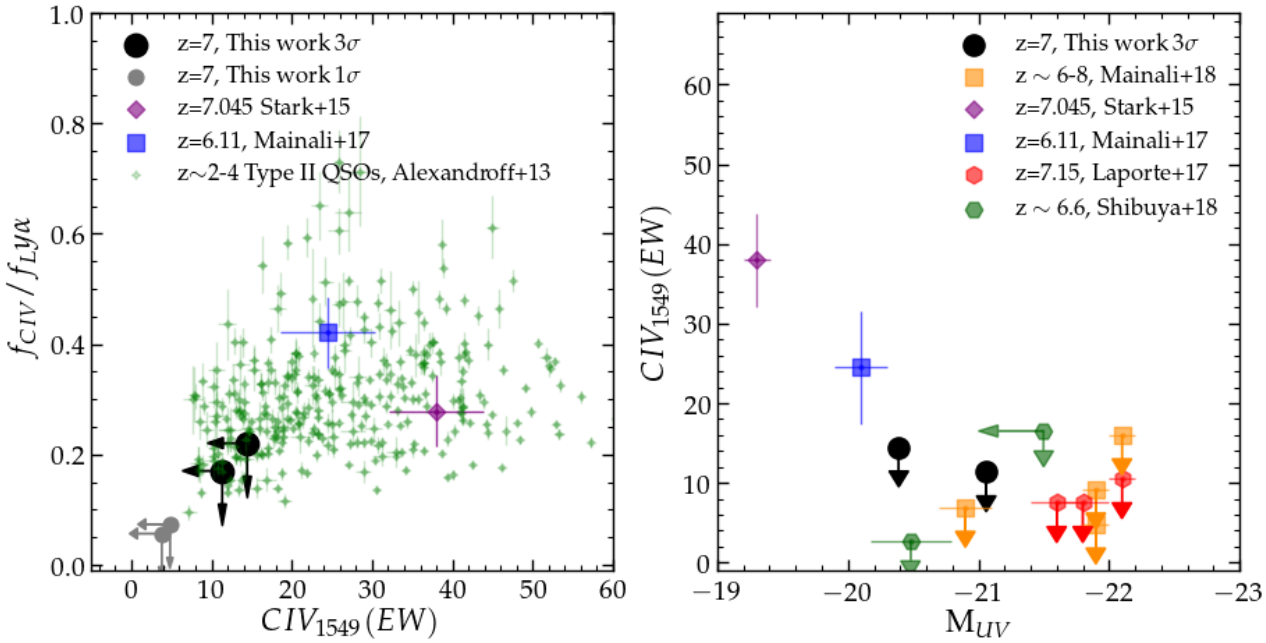

Fig. 2. *Left*: position of BDF521 and BDF2195 on the $f_{\rm CIV}/f_{\rm Ly\alpha}$ vs. Lyα(EW) plane compared to $z \gtrsim 6$ objects with detected CIV emission (Stark et al. 2015b; Mainali et al. 2017), and to Type II QSOs at intermediate redshift from Alexandroff et al. (2013). *Right*: position of the BDF LAEs on the CIV(EW) vs. $M_{\rm UV}$ plane compared to $z \gtrsim 6$ sources from the literature including upper limits from Laporte et al. (2017), Mainali et al. (2018), and Shibuya et al. (2018). All upper limits are at 3σ. See the legend for symbols and colours.

4. Limits on the contribution from AGN emission

The analysis of the limits on CIV emission presented in Fig. 2, and the existing constraints on the Lyα/NV ratio (C18), already suggest that it is unlikely the BDF emitters are dominated by AGN emission.

We performed a more quantitative analysis by comparing the limits on CIV and HeII emission against the narrow-line AGN models by Feltre et al. (2016). We considered models with $-5.0 \leq \log(U_{\rm s}) \leq -1.0$ and interstellar gas metallicity $Z = 0.025, 0.1, 0.4\,Z_{\odot}$, dust-to-metal mass ratio $\xi_{\rm d} = 0.3$, and hydrogen gas density $n_{\rm H} = 100\,{\rm cm}^{-3}$. We restricted our analysis to models generated with incident spectra that had a UV spectral index $\alpha = -1.7$, but we verified that results did not significantly change when adopting spectra with index $\alpha = -1.4$. We first re-normalized the incident spectra to a chosen fraction of the observed flux of each object in the $F125W$ filter (C16) (i.e., the observable non-ionizing UV flux at ∼1500 Å) and then computed the EWs of the CIV and HeII lines on the basis of the predicted line flux for each model and of the observed flux at the relevant wavelength. We note that using the models in this way allows us to constrain scenarios in which the AGN emission is contributing to the UV continuum emission, which is the most important test for constraining the ionizing output of our targets. While the models do not include the broad line region emission, this is not a concern in our case, given the narrow FWHM of the Lyα lines observed in the BDF galaxies. We show in Fig. 3 the position on the CIV(EW) vs. the HeII(EW) plane of AGN models with a 40%, 60%, and 100% contribution to the observed UV emission highlighting the regions allowed at 1σ, 2σ, and 3σ by the X-shooter observations. Models with pure AGN (100%) are always excluded at $\gtrsim 2{-}3\sigma$ regardless of $\log(U_{\rm s})$ and metallicity. The more stringent constraints on BDF2195 allow us to also exclude a 60% AGN contribution at $\sim 3\sigma$. Models with 40% contribution are more compatible with the observations, particularly for BDF521, for high $\log(U_{\rm s})$ and intermediate and high metallicities.

The narrow-line models of Feltre et al. (2016) can be further used to investigate the case of an obscured AGN that provides no contribution to the UV continuum emission. In such a case, we must consider the fractional contribution of the AGN to the observed Lyα emission. Since the radiative transfer effects of Lyα are severe, we investigate what fraction of Lyα can escape for a given fractional contribution of AGN without the measured line limits being invalidated. For a similar parameter space of the models investigated above, we find that we can only rule out 100% narrow-line region contribution to Lyα if only 20% (15%) escapes for BDF2195 (BDF521). For a lower escape fraction of Lyα, the line contribution can have 100% contribution from a Type-II AGN without the other rest-frame UV lines being detected.

5. The ionizing emission budget of the BDF emitters

From the above analysis it appears that the BDF pair lacks high-ionization features found in some other sources at a similar redshift, and instead resembles standard star-forming galaxies at lower redshifts with low or absent contribution from AGN. We thus constrain the physical parameters of the two galaxies, including the ionizing budget, by means of a spectro-photometric fit performed with the BEAGLE v0.24.5 tool (Chevallard & Charlot 2016), using the most recent version of the Bruzual & Charlot (2003) stellar population synthesis models (see Vidal-García et al. 2017, for details). Nebular emission is modelled self-consistently as described in Gutkin et al. (2016) by processing stellar emission with the photoionization code CLOUDY (c13.03, Ferland et al. 2013). The fit is performed by fitting the upper limits on the integrated lines plus continuum fluxes measured as described in Sect. 3, together with the broad-band photometric measurements redwards of the Lyman break in the $F105W$, $F125W$, $F160W$, and HAWK-I Ks bands (C16, see also Castellano et al. 2010; Cai et al. 2015). Given that the

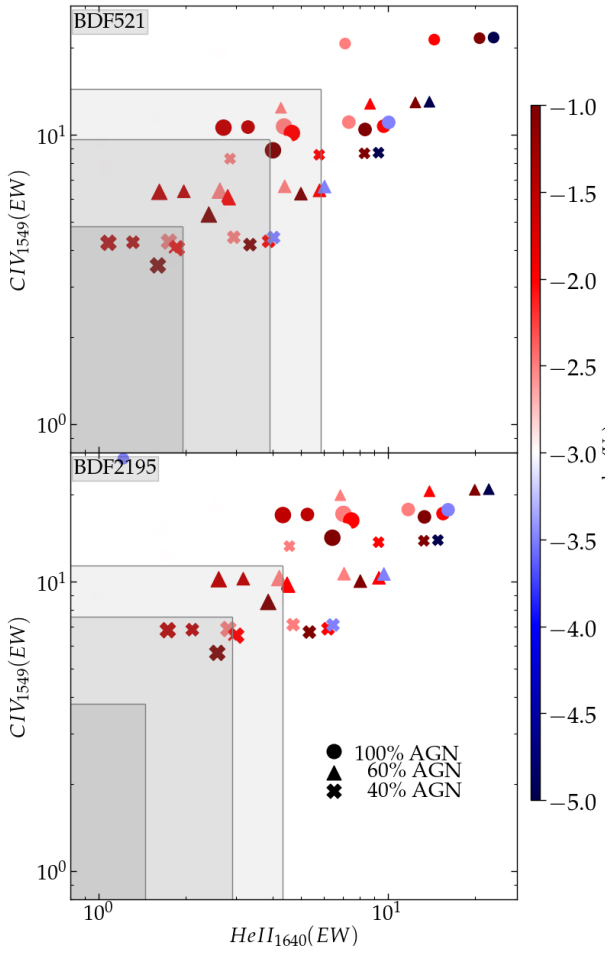

Fig. 3. Position in the CIV(EW) vs. HeII(EW) plane of models with 40% (crosses), 60% (triangles) and 100% (circles) contribution to the observed UV emission of the two BDF galaxies from narrow-line AGN (from Feltre et al. 2016) with different metallicities and ionization parameters. Symbols at increasing sizes are for models with $Z = 0.025$, 0.1, $0.4\,Z_\odot$, whose colour indicate the relevant ionization parameter $\log(U_s)$. The shaded regions highlight the parameter space allowed at 1σ, 2σ, and 3σ by the X-shooter observations of BDF521 (*top*) and BDF2195 (*bottom*).

Lyα is very difficult to model in this framework, we subtracted its flux from the affected bands and did not include it in the nebular emission modelled by BEAGLE. We fixed the redshift at the value determined from Lyα. Although there is usually a shift between Lyα and systemic redshift, this, in practice, has no effect on the constraints derived here. The BEAGLE spectral energy distribution (SED) fitting runs were performed with a configuration similar to that discussed by Stark et al. (2017). The templates are based on a Chabrier (2003) initial mass function and have metallicity in the range $-2.2 \leq \log(Z/Z_\odot) \leq 0.25$. The star-formation histories (SFHs) are parametrized as an exponentially delayed function (SFR(t) $\propto t \cdot \exp(-t/\tau)$), which is the most flexible parametric SFH allowed by the code, plus an ongoing constant burst with a duration of 10 Myr. We adopted uniform priors on the SFH exponential timescale ($7.0 \leq \tau/\log(\mathrm{yr}) \leq 10.5$), stellar mass ($7.0 \leq \log(M/M_\odot) \leq 12$), and maximum stellar age ($7.0 \leq \log(\mathrm{Age/yr}) \leq$ age of the Universe). Attenuation by dust is treated following the Charlot & Fall (2000) model combined with the Chevallard et al. (2013) prescriptions for geometry and inclination effects, assuming an effective V-band optical depth in the range $-3.0 \leq \log(\tau_V) \leq 0.7$ with a fixed fraction $\mu = 0.4$ arising from dust in the diffuse ISM. Interstellar metallicity $Z_{\rm ISM}$ is assumed to be identical to the stellar one, and the dust-to-metal mass ratio and ionization parameter are left free in the ranges $0.1 \leq \xi_d \leq 0.5$ and $-4.0 \leq \log(U_s) \leq -1.0$, respectively.

Table 2. Properties of the BDF pair.

	BDF521	BDF2195
Redshift	7.0121	7.0124
$M_{\rm UV}$	−20.4	−21.1
UV slope	-2.25 ± 0.25	-1.66 ± 0.16
$M_{\rm star}$ ($10^9\,M_\odot$)	$1.04^{+0.48}_{-0.40}$	$2.67^{+1.11}_{-1.19}$
SFR ($M_\odot\,\mathrm{yr}^{-1}$)	$14.9^{+4.8}_{-5.4}$	$16.0^{+9.5}_{-9.8}$
Age [(a)] (Myr)	23^{+5}_{-12}	34^{+20}_{-20}
Stellar $Z/Z_\odot$ [(a)]	$0.14^{+0.15}_{-0.13}$	$0.12^{+0.11}_{-0.11}$
A_{1500} (mag)	$1.4^{+0.40}_{-0.40}$	$1.4^{+0.38}_{-0.40}$
$\xi^*_{\rm ion}$ (log(erg/Hz))	$25.26^{+0.1}_{-0.1}$	$25.02^{+0.22}_{-0.22}$

Notes. Physical properties (mean values and 68% c.l. uncertainties) are from the BEAGLE spectro-photometric fit. [(a)]Mass-weighted values.

We exploited the observed Lyα flux to impose a prior on the ongoing SFR. Following Kennicutt (1998), the total line fluxes correspond to SFR(Lyα) $= 6.7 \pm 0.5\,M_\odot\,\mathrm{yr}^{-1}$ for BDF521 and SFR(Lyα) $= 11.4 \pm 0.6\,M_\odot\,\mathrm{yr}^{-1}$ for BDF2195. As we expected the SFR inferred from the detected Lyα to be a lower limit to the intrinsic SFR of BDF521 and BDF2195, depending on their Lyα escape fraction and attenuation by the IGM, we used the corresponding 5σ lower limits on SFR(Lyα), that is to say $\simeq 4\,M_\odot\,\mathrm{yr}^{-1}$ and $\simeq 8\,M_\odot\,\mathrm{yr}^{-1}$, as conservative lower bounds for the uniform prior ranges on their current SFRs.

The best-fit parameters and relevant 68% confidence level uncertainties are shown in Table 2. The objects are found to be relatively young (mass-weighted age ∼20–30 yr^{-1} Myr) and metal-poor ($\lesssim 0.3\,Z_\odot$) galaxies, with stellar masses of a few $10^9\,M_\odot$. Both objects are actively star-forming (SFR $\sim 15\,M_\odot\,\mathrm{yr}^{-1}$), but had experienced a higher star-formation activity in the past. We find a small degeneracy among the mass, extinction and age parameters, with older models being more massive and less extincted by dust. The results do not change significantly when adopting different parametrizations of the SFH, nor with the updated treatment of dust within HII regions implemented in BEAGLE v0.27.1 and described in Curtis-Lake et al. (2021).

The most important parameter to explore thanks to the combined spectroscopic and photometric information is the production rate of hydrogen ionizing photons per intrinsic (i.e., unattenuated) UV luminosity, $\xi^*_{\rm ion}$. We find best-fit values for $\log(\xi^*_{\rm ion}/\mathrm{Hz\,erg}^{-1})$ of 25.26 for BDF521 and 25.02 for BDF2195. These values are consistent with the typical ionizing production efficiency of $z \gtrsim 4$ populations (Bouwens et al. 2015a, 2016; Lam et al. 2019), and significantly lower than the $\log(\xi^*_{\rm ion}/\mathrm{Hz\,erg}^{-1}) \simeq 25.6$–25.7 found in $z > 7$ galaxies with CIII] detection and/or photometric evidence of strong optical emission lines (Stark et al. 2015b, 2017). The ionizing emission from the BDF emitters is lower, albeit consistent at $\sim 1\sigma$, with the average value in $z \sim 5$ LAEs (Harikane et al. 2018) and with the $\log(\xi^*_{\rm ion}/\mathrm{Hz\,erg}^{-1}) = 25.43$ estimated for the BDF galaxies by Rodríguez Espinosa et al. (2021) on the basis of the Lyα luminosity following Sobral & Matthee (2019). Most importantly,

these results show that the two emitters are 'standard' high-redshift star-forming galaxies, with no significant excess production of ionizing photons contributing to the local reionization history.

With the improved constraints coming from the new spectro-photometric fit described in the previous section, we can quantitatively explore whether the BDF pair is capable of reionizing its surroundings or not. The SFR and the age of a galaxy can be used to measure the size ($R_{\rm bubble}$) of the resulting ionized region following, for example, Shapiro & Giroux (1987) and Madau et al. (1999), by assuming an escape fraction of ionizing photons $f_{\rm esc}$, the hydrogen clumping factor C, and an average neutral hydrogen fraction $\chi_{\rm HI}$ at the onset of star formation. As discussed in V11 and C18, the size $R_{\rm bubble}$ must then be compared to the minimum size $R_{\rm min}$ = 1.1 Mpc, enabling Lyα to be redshifted enough to reach the observers (Wyithe & Loeb 2005). The aforementioned $R_{\rm min}$ is found under the assumption that the Lyα escapes from the galaxies at the systemic redshift. The size threshold decreases in the presence of strong outflows, for example a 220 km s^{-1} shift, which is the median value found by Mason et al. (2018) (see also Endsley et al. 2022) for galaxies in massive halos, resulting in $R_{\rm min} \sim 0.85$ Mpc.

In practice, we computed the average SFR of the pair from all models within 95% c.l. from the best fit as a function of time in bins of 5 Myr. We then converted this into $R_{\rm bubble}$ by assuming $C = 2$ and $\chi_{\rm HI} = 0.5$, and let the escape fraction $f_{\rm esc}$ vary from 10% to 80%. The assumption of a 50% neutral fraction is conservative as a higher $\chi_{\rm HI}$ would further decrease the size of the reionized region created by the sources. The results are shown in Fig. 4 as a function of the relevant maximum stellar age of the models (i.e., the onset of the star-formation episode). We find that in the absence of significant outflows, only models with an extremely high $f_{\rm esc}$ = 80% and older than 200 Myr (formation redshift $z > 9$) can create a large enough bubble.

When assuming a Lyα shift imprinted by 220 km s^{-1} outflows, the two objects could grow a large enough bubble with an escape fraction $f_{\rm esc}$ = 40% in the same time frame. However, even in the presence of outflows, there are no spectro-photometric fitting solutions that would allow the BDF pair to reionize the surrounding region with an escape fraction of $f_{\rm esc}$ = 10%. This is particularly relevant when considering that the physical properties of the BDF galaxies, that is to say the moderate $\xi^*_{\rm ion}$, and low EW of the UV metal lines, are typical for galaxies with low $f_{\rm esc}$ (Naidu et al. 2022). It should be noted that these results are considerably more stringent than those discussed in C18 based solely on the SED fitting of the available photometry. The C18 results were consistent with a combination of high SFRs and old ages, which in turn allowed the formation of a large enough reionized bubble. Our current spectro-photometric analysis suggests that the two emitters are not solely responsible for the growth of the ionized bubble. In turn, this finding is consistent with the analysis of the BDF region presented by Rodríguez Espinosa et al. (2021), indicating that a dominant contribution is provided by the clustered faint galaxies.

6. Summary and future prospects

We have presented the analysis of deep VLT X-shooter observations of BDF521 and BDF2195, a pair of $L \sim L^*$, bright Lyα emitting galaxies at ~90 kpc separation shining within the BDF bubble, which is an overdensity of both LBGs and LAEs at $z \sim 7$, showing all expected properties of a 'reionized bubble' embedded in a half-neutral Universe (V11, C16, C18, Rodríguez Espinosa et al. 2021). Our main findings can be summarized as follows:

- The Lyα lines are detected at high significance in the VIS arm spectra at $z = 7.0121$ for BDF521 and $z = 7.0124$ for BDF2195. The Lyα properties (EW $\simeq$ 60 Å and FWHM $\simeq$ 250–260 km s^{-1}) are consistent with previous analyses based on lower resolution FORS2 spectra.
- No significant emission is detected in the NIR arm spectra at the expected position of the CIVλ1548 doublet, HeIIλ1640, the OIII]λ1660 doublet, and the CIII]λ1909 doublet. We can place stringent 3σ upper limits on the EW of each line or doublet component in the range ~2–7 Å (Table 1).
- A comparison with other high-redshift sources from the literature shows that our two BDF emitters have lower CIII] emission than expected, on the basis of the average correlation between the Lyα and CIII] EWs measured at lower redshifts, although they are consistent with being at the lower envelope of the measured distributions (Fig. 1).
- Although an AGN contribution cannot be completely ruled out, the constraints on the CIV(EW) and the flux ratio $f_{\rm CIV}/f_{\rm Ly\alpha}$ (Fig. 2) show that the objects are only marginally consistent with them being AGN when compared to known Type II QSOs at lower redshifts. Consistently, when comparing limits on the HeII(EW) and CIV(EW) planes to narrow-line AGN models by Feltre et al. (2016), we can exclude pure AGN (100%) templates at ~2–3σ. Instead, models with a $\lesssim$40% AGN contribution could be compatible with the observations (Fig. 3).
- A spectro-photometric fit on the available data indicates that the two objects are relatively young (~20–30 Myr) and metal-poor ($\lesssim 0.3\,Z_\odot$) with stellar masses of a few $10^9\,M_\odot$ (Table 2). Most importantly, we find a production rate of hydrogen ionizing photons per intrinsic UV luminosity of $\log(\xi^*_{\rm ion}/{\rm Hz\,erg^{-1}}) = 25.02$–$25.26$ (under the assumption of a purely stellar origin). This is consistent with the value typically found in high-redshift populations, but significantly lower than the extreme values ($\simeq$25.6–25.7) measured in $z > 7$ galaxies with CIII] detection (Stark et al. 2015b) or with evidence of strong optical emission lines from their mid-IR photometry (Stark et al. 2017).
- The range of physical parameters allowed by the spectro-photometric fit does not allow the BDF pair to reionize their surroundings by themselves with a low or even a moderate escape fraction of ionizing photons, as they would require extremely high $f_{\rm esc}$ = 40% and need to be older than 200 Myr (formation redshift $z > 9$) (Fig. 4).

The results summarized above indicate that the two emitters are typical high-redshift sources with no peculiar ionizing capabilities, either due to extreme stellar populations or to a significant contribution from AGN emission. The low metal line emission and the moderate $\xi^*_{\rm ion}$ are likely explained by a combination of low metallicity and the galaxies being caught in a quiet phase of star-formation activity. In addition, the lack of a significant AGN contribution is not surprising in light of theoretical predictions showing a dominant contribution from star formation to the UV emission of bright high-redshift galaxies (Piana et al. 2022). Most importantly for our purposes, it is unlikely that they are solely responsible for the growth of the ionized bubble. Instead, a dominant contribution to the local reionization history can be provided by the overdensity of faint galaxies.

These findings allow us to draw a plan for future observations that would be capable of fully constraining the properties of this remarkable region. Presently, the most important

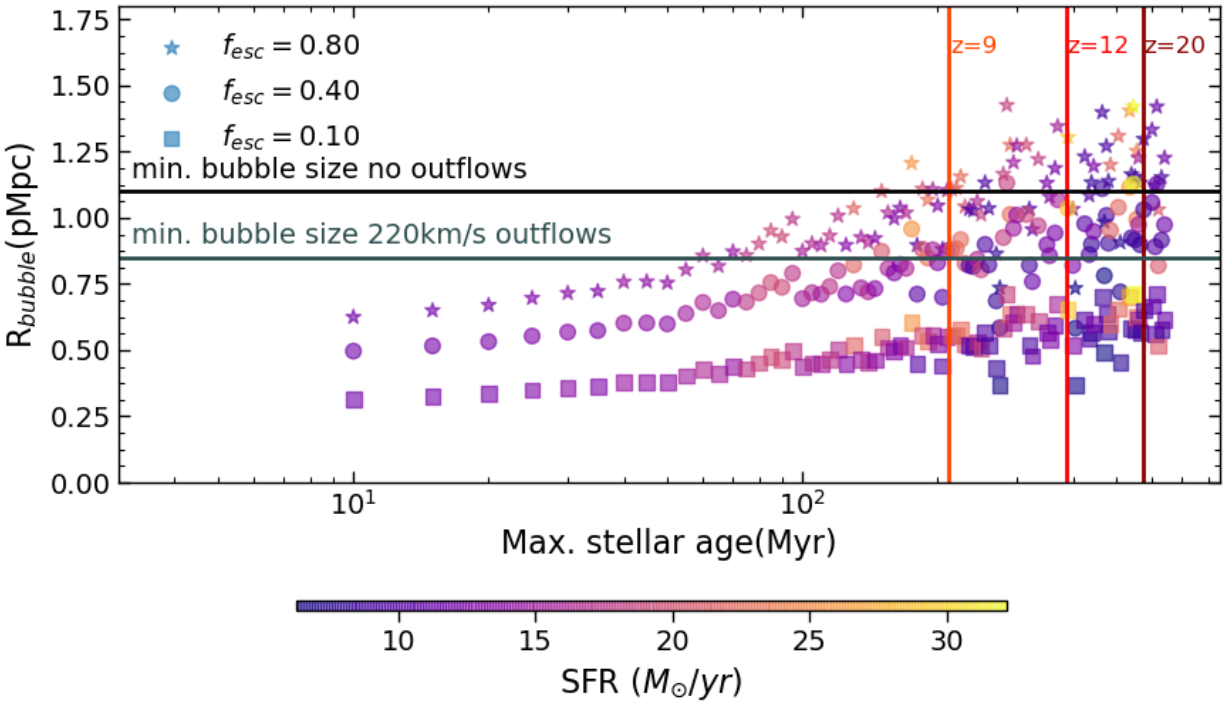

Fig. 4. Size ($R_{\rm bubble}$) of the ionized bubble created by the combined emission of the BDF pair, as a function of the maximum stellar age of the stellar population for BEAGLE SED models within 95% c.l. from the best fit. The cases for escape fraction $f_{\rm esc}$ = 0.1,0.4, and 0.8 are shown as squares, circles, and stars, respectively, with colour indicating the relevant, total, SFR of the system. The horizontal black line marks the minimum HII size $R_{\rm min}$ = 1.1 Mpc that would enable Lyα to escape. The dark grey line indicates the minimum HII size $R_{\rm min}$ = 0.85 Mpc in the case Lyα is affected by a 220 km s^{-1} outflow. Vertical lines, from left to right, indicate formation redshifts z = 9, 12, and 20.

missing ingredient to confirm that the overdensity of faint galaxies reionized the BDF region is their spectroscopic confirmation. Given the absence of strong Lyα emission, this is beyond the capabilities of ground-based telescopes, and attempting detection of sub-millimetre lines with the Atacama Large Millimeter/submillimeter Array in redshift scan mode would be exceedingly time consuming. However, spectroscopic confirmation is well within the capabilities of the *James Webb* Space Telescope (JWST). Indeed, JWST-NIRSpec in ∼1.5 h of integration time could detect [OIII]λ4959, 5007 from all currently known candidates down to $M_{\rm UV} \simeq -19$, while also fully constraining the ionization state and metallicity of the LAEs through the detection of [OII]λ3727 and Hβ. In addition, the JWST can extend the photometric mapping of the BDF in terms of area, depth, and wavelength coverage to confirm the presence of an overdensity of LBGs down to fainter magnitudes. For example, ∼1–2 h of NIRCam integration per filter can extend the constraints on the local UV LF down to $M_{\rm UV} \sim -18.0$ while covering the optical rest-frame wavelength range, which is crucial in order to reject low-redshift interlopers and constrain the spectral energy distributions.

Finally, a significant contribution to our understanding of the formation of reionized regions will be provided by objects beyond the limit that can be reached on blank fields such as the BDF, for example, objects analogous to the $z \sim 6$ clustered ultra-faint dwarfs observed by Vanzella et al. (2019) (see also Vanzella et al. 2021b). In this respect, JWST surveys on lensed fields (Treu et al. 2017; Willott et al. 2017; Vanzella et al. 2021a) will provide crucial information, such as an accurate characterization of the faintest end of the UV LF and of its possible turnover (e.g., Castellano et al. 2016b; Yue et al. 2018), and of the physical properties of high-redshift ultra-faint dwarfs (e.g., Vanzella et al. 2017a,b).

With the sample of candidate reionized regions steadily growing, the advent of the JWST will enable a systematic investigation of the connection between the physical properties of high-redshift galaxies and the ionization state of the surrounding IGM, eventually providing an answer as to the sources of reionization.

Acknowledgements. Based on observations collected at the European Southern Observatory for Astronomical research in the Southern Hemisphere under ESO programme 0103.A-0710. We thank A. Feltre for the useful discussions and support on the use of the narrow-line AGN models. ECL acknowledges support of an STFC Webb Fellowship (ST/W001438/1). EV acknowledges funding from the INAF for "interventi aggiuntivi a sostegno della ricerca di main-stream" and PRIM-MIUR 2017WSCC32 "Zooming into dark matter and proto-galaxies with massive lensing clusters". RA acknowledges support from ANID FONDECYT Regular Grant 1202007. PD and AH acknowledge support from the European Research Council's starting grant ERC StG-717001 ("DELPHI"). PD acknowledges support from the NWO grant 016.VIDI.189.162 ("ODIN") and the European Commission's and University of Groningen's CO-FUND Rosalind Franklin program. A. Ferrara and S. Carniani acknowledge support from the ERC Advanced Grant INTERSTELLAR H2020/740120. Partial support from the Carl Friedrich von Siemens-Forschungspreis der Alexander von Humboldt-Stiftung Research Award is kindly acknowledged. This research made use of the MATPLOTLIB package (https://matplotlib.org/) (Hunter 2007), of ASTROPY (http://www.astropy.org), a community-developed core Python package for Astronomy (Astropy Collaboration 2013, 2018), and of the SPECUTILS package (https://specutils.readthedocs.io/en/stable/).

References

Alexandroff, R., Strauss, M. A., Greene, J. E., et al. 2013, MNRAS, 435, 3306
Amorín, R., Fontana, A., Pérez-Montero, E., et al. 2017, Nat. Astron., 1, 0052
Astropy Collaboration (Price-Whelan, A. M., et al.) 2018, AJ, 156, 123
Astropy Collaboration (Robitaille, T. P., et al.) 2013, A&A, 558, A33
Bañados, E., Venemans, B. P., Mazzucchelli, C., et al. 2018, Nature, 553, 473
Berg, D. A., Erb, D. K., Henry, R. B. C., Skillman, E. D., & McQuinn, K. B. W. 2019, ApJ, 874, 93

Boutsia, K., Grazian, A., Giallongo, E., et al. 2011, ApJ, 736, 41
Bouwens, R. J., Illingworth, G. D., Oesch, P. A., et al. 2015a, ApJ, 811, 140
Bouwens, R. J., Illingworth, G. D., Oesch, P. A., et al. 2015b, ApJ, 803, 34
Bouwens, R. J., Smit, R., Labbé, I., et al. 2016, ApJ, 831, 176
Bruzual, G., & Charlot, S. 2003, MNRAS, 344, 1000
Cai, Z., Fan, X., Jiang, L., et al. 2015, ApJ, 799, L19
Calabrò, A., Amorín, R., Fontana, A., et al. 2017, A&A, 601, A95
Castellano, M., Fontana, A., Paris, D., et al. 2010, A&A, 524, A28
Castellano, M., Fontana, A., Grazian, A., et al. 2012, A&A, 540, A39
Castellano, M., Dayal, P., Pentericci, L., et al. 2016a, ApJ, 818, L3
Castellano, M., Yue, B., Ferrara, A., et al. 2016b, ApJ, 823, L40
Castellano, M., Pentericci, L., Vanzella, E., et al. 2018, ApJ, 863, L3
Chabrier, G. 2003, PASP, 115, 763
Charlot, S., & Fall, S. M. 2000, ApJ, 539, 718
Chevallard, J., & Charlot, S. 2016, MNRAS, 462, 1415
Chevallard, J., Charlot, S., Wandelt, B., & Wild, V. 2013, MNRAS, 432, 2061
Chevallard, J., Charlot, S., Senchyna, P., et al. 2018, MNRAS, 479, 3264
Choudhury, T. R., Haehnelt, M. G., & Regan, J. 2009, MNRAS, 394, 960
Cupani, G., D'Odorico, V., Cristiani, S., et al. 2020, in SPIE Conf. Ser., 11452, 114521U
Curtis-Lake, E., Chevallard, J., Charlot, S., & Sandles, L. 2021, MNRAS, 503, 4855
Dayal, P., & Ferrara, A. 2018, Phys. Rep., 780, 1
Dayal, P., Ferrara, A., Saro, A., et al. 2009, MNRAS, 400, 2000
Dayal, P., Maselli, A., & Ferrara, A. 2011, MNRAS, 410, 830
Dayal, P., Volonteri, M., Choudhury, T. R., et al. 2020, MNRAS, 495, 3065
de Barros, S., Vanzella, E., Amorín, R., et al. 2016, A&A, 585, A51
Dijkstra, M. 2019, Saas-Fee Advanced Course, 46, 1
Duncan, K., & Conselice, C. J. 2015, MNRAS, 451, 2030
Endsley, R., & Stark, D. P. 2022, MNRAS, 511, 6042
Endsley, R., Stark, D. P., Charlot, S., et al. 2021a, MNRAS, 502, 6044
Endsley, R., Stark, D. P., Chevallard, J., & Charlot, S. 2021b, MNRAS, 500, 5229
Endsley, R., Stark, D. P., Bouwens, R. J., et al. 2022, MNRAS, submitted [arXiv:2202.01219]
Fan, X., Narayanan, V. K., Strauss, M. A., et al. 2002, AJ, 123, 1247
Feltre, A., Charlot, S., & Gutkin, J. 2016, MNRAS, 456, 3354
Ferland, G. J., Porter, R. L., van Hoof, P. A. M., et al. 2013, Rev. Mex. Astron. Astrofis., 49, 137
Finkelstein, S. L., D'Aloisio, A., Paardekooper, J.-P., et al. 2019, ApJ, 879, 36
Flury, S. R., Jaskot, A. E., Ferguson, H. C., et al. 2022, ApJS, 260, 1
Fontana, A., Vanzella, E., Pentericci, L., et al. 2010, ApJ, 725, L205
Giallongo, E., Grazian, A., Fiore, F., et al. 2015, A&A, 578, A83
Grazian, A., Giallongo, E., Paris, D., et al. 2017, A&A, 602, A18
Greig, B., & Mesinger, A. 2017, MNRAS, 465, 4838
Gutkin, J., Charlot, S., & Bruzual, G. 2016, MNRAS, 462, 1757
Hainline, K. N., Shapley, A. E., Greene, J. E., & Steidel, C. C. 2011, ApJ, 733, 31
Harikane, Y., Ouchi, M., Shibuya, T., et al. 2018, ApJ, 859, 84
Harikane, Y., Ono, Y., Ouchi, M., et al. 2022, ApJS, 259, 20
Higuchi, R., Ouchi, M., Ono, Y., et al. 2019, ApJ, 879, 28
Humphrey, A., Villar-Martín, M., Vernet, J., et al. 2008, MNRAS, 383, 11
Hunter, J. D. 2007, Comput. Sci. Eng., 9, 90
Hutchison, T. A., Papovich, C., Finkelstein, S. L., et al. 2019, ApJ, 879, 70
Hutter, A., Dayal, P., & Müller, V. 2015, MNRAS, 450, 4025
Hutter, A., Dayal, P., Yepes, G., et al. 2021, MNRAS, 503, 3698
Ishigaki, M., Kawamata, R., Ouchi, M., et al. 2018, ApJ, 854, 73
Izotov, Y. I., Schaerer, D., Worseck, G., et al. 2018a, MNRAS, 474, 4514
Izotov, Y. I., Worseck, G., Schaerer, D., et al. 2018b, MNRAS, 478, 4851
Jiang, L., Kashikawa, N., Wang, S., et al. 2021, Nat. Astron., 5, 256
Jung, I., Papovich, C., Finkelstein, S.L., et al. 2021, ApJ, submitted [arXiv:2111.14863]
Kennicutt, R. C., Jr 1998, ARA&A, 36, 189
Lam, D., Bouwens, R. J., Labbé, I., et al. 2019, A&A, 627, A164
Laporte, N., Nakajima, K., Ellis, R. S., et al. 2017, ApJ, 851, 40
Le Fèvre, O., Lemaux, B. C., Nakajima, K., et al. 2019, A&A, 625, A51
Lehnert, M. D., & Bremer, M. 2003, ApJ, 593, 630
Lemaux, B. C., Lubin, L. M., Sawicki, M., et al. 2009, ApJ, 700, 20
Lenz, D. D., & Ayres, T. R. 1992, PASP, 104, 1104
Leonova, E., Oesch, P. A., Qin, Y., et al. 2021, MNRAS, submitted [arXiv:2112.07675]
Livermore, R. C., Finkelstein, S. L., & Lotz, J. M. 2017, ApJ, 835, 113
Llerena, M., Amorín, R., Cullen, F., et al. 2022, A&A, 659, A16
Madau, P., Haardt, F., & Rees, M. J. 1999, ApJ, 514, 648
Mainali, R., Kollmeier, J. A., Stark, D. P., et al. 2017, ApJ, 836, L14
Mainali, R., Zitrin, A., Stark, D. P., et al. 2018, MNRAS, 479, 1180
Maiolino, R., Carniani, S., Fontana, A., et al. 2015, MNRAS, 452, 54
Malhotra, S., & Rhoads, J. E. 2006, ApJ, 647, L95
Marchi, F., Pentericci, L., Guaita, L., et al. 2017, A&A, 601, A73
Marchi, F., Pentericci, L., Guaita, L., et al. 2019, A&A, 631, A19
Mason, C. A., Treu, T., de Barros, S., et al. 2018, ApJ, 857, L11
Mason, C. A., Fontana, A., Treu, T., et al. 2019, MNRAS, 485, 3947
Mitra, S., Choudhury, T. R., & Ferrara, A. 2015, MNRAS, 454, L76
Mitra, S., Choudhury, T. R., & Ferrara, A. 2018, MNRAS, 473, 1416
Modigliani, A., Goldoni, P., Royer, F., et al. 2010, in Observatory Operations: Strategies, Processes, and Systems III, eds. D. R. Silva, A. B. Peck, & B. T. Soifer, SPIE Conf. Ser., 7737, 773728
Naidu, R. P., Oesch, P. A., Reddy, N., et al. 2017, ApJ, 847, 12
Naidu, R. P., Matthee, J., Oesch, P. A., et al. 2022, MNRAS, 510, 4582
Nakajima, K., Ellis, R. S., Iwata, I., et al. 2016, ApJ, 831, L9
Nakajima, K., Fletcher, T., Ellis, R. S., Robertson, B. E., & Iwata, I. 2018a, MNRAS, 477, 2098
Nakajima, K., Schaerer, D., Le Fèvre, O., et al. 2018b, A&A, 612, A94
Oesch, P. A., Brammer, G., van Dokkum, P. G., et al. 2016, ApJ, 819, 129
Oesch, P. A., Bouwens, R. J., Illingworth, G. D., Labbé, I., & Stefanon, M. 2018, ApJ, 855, 105
Oke, J. B., & Gunn, J. E. 1983, ApJ, 266, 713
Ono, Y., Ouchi, M., Mobasher, B., et al. 2012, ApJ, 744, 83
Pahl, A. J., Shapley, A., Steidel, C. C., Chen, Y., & Reddy, N. A. 2021, MNRAS, 505, 2447
Pallottini, A., Ferrara, A., Decataldo, D., et al. 2019, MNRAS, 487, 1689
Pentericci, L., Fontana, A., Vanzella, E., et al. 2011, ApJ, 743, 132
Pentericci, L., Vanzella, E., Fontana, A., et al. 2014, ApJ, 793, 113
Pentericci, L., McLure, R. J., Garilli, B., et al. 2018, A&A, 616, A174
Piana, O., Dayal, P., & Choudhury, T. R. 2022, MNRAS, 510, 5661
Planck Collaboration VI. 2020, A&A, 641, A6
Rigby, J. R., Bayliss, M. B., Gladders, M. D., et al. 2015, ApJ, 814, L6
Robertson, B. E., Ellis, R. S., Furlanetto, S. R., & Dunlop, J. S. 2015, ApJ, 802, L19
Rodríguez Espinosa, J. M., Mas-Hesse, J. M., & Calvi, R. 2021, MNRAS, 503, 4242
Romanello, M., Menci, N., & Castellano, M. 2021, Universe, 7, 365
Schenker, M. A., Stark, D. P., Ellis, R. S., et al. 2012, ApJ, 744, 179
Schmidt, K. B., Huang, K. H., Treu, T., et al. 2017, ApJ, 839, 17
Schmidt, K. B., Kerutt, J., Wisotzki, L., et al. 2021, A&A, 654, A80
Shapiro, P. R., & Giroux, M. L. 1987, ApJ, 321, L107
Shibuya, T., Ouchi, M., Harikane, Y., et al. 2018, PASJ, 70, S15
Shivaei, I., Reddy, N. A., Siana, B., et al. 2018, ApJ, 855, 42
Sobacchi, E., & Mesinger, A. 2015, MNRAS, 453, 1843
Sobral, D., & Matthee, J. 2019, A&A, 623, A157
Stark, D. P., Ellis, R. S., Chiu, K., Ouchi, M., & Bunker, A. 2010, MNRAS, 408, 1628
Stark, D. P., Richard, J., Siana, B., et al. 2014, MNRAS, 445, 3200
Stark, D. P., Richard, J., Charlot, S., et al. 2015a, MNRAS, 450, 1846
Stark, D. P., Walth, G., Charlot, S., et al. 2015b, MNRAS, 454, 1393
Stark, D. P., Ellis, R. S., Charlot, S., et al. 2017, MNRAS, 464, 469
Steidel, C. C., Bogosavljević, M., Shapley, A. E., et al. 2018, ApJ, 869, 123
Tang, M., Stark, D. P., Chevallard, J., & Charlot, S. 2019, MNRAS, 489, 2572
Tilvi, V., Pirzkal, N., Malhotra, S., et al. 2016, ApJ, 827, L14
Tilvi, V., Malhotra, S., Rhoads, J. E., et al. 2020, ApJ, 891, L10
Topping, M. W., Shapley, A. E., Stark, D. P., et al. 2021, ApJ, 917, L36
Trebitsch, M., Dubois, Y., Volonteri, M., et al. 2021, A&A, 653, A154
Treu, T., Trenti, M., Stiavelli, M., Auger, M. W., & Bradley, L. D. 2012, ApJ, 747, 27
Treu, T. L., Abramson, L. E., Bradac, M., et al. 2017, Through the Looking GLASS: A JWST Exploration of Galaxy Formation and Evolution from Cosmic Dawn to Present Day, JWST Proposal ID 1324. Cycle 0 Early Release Science
Vanzella, E., Pentericci, L., Fontana, A., et al. 2011, ApJ, 730, L35
Vanzella, E., de Barros, S., Vasei, K., et al. 2016, ApJ, 825, 41
Vanzella, E., Calura, F., Meneghetti, M., et al. 2017a, MNRAS, 467, 4304
Vanzella, E., Castellano, M., Meneghetti, M., et al. 2017b, ApJ, 842, 47
Vanzella, E., Nonino, M., Cupani, G., et al. 2018, MNRAS, 476, L15
Vanzella, E., Calura, F., Meneghetti, M., et al. 2019, MNRAS, 483, 3618
Vanzella, E., Caminha, G. B., Calura, F., et al. 2020, MNRAS, 491, 1093
Vanzella, E., Adamo, A., Annibali, F., et al. 2021a, Constraining the Nature of the First Stellar Complexes: Globular Cluster Precursors and Population III Stellar Clusters at z 6–7, JWST Proposal. Cycle 1
Vanzella, E., Caminha, G. B., Rosati, P., et al. 2021b, A&A, 646, A57
Vidal-García, A., Charlot, S., Bruzual, G., & Hubeny, I. 2017, MNRAS, 470, 3532
Watson, D., Christensen, L., Knudsen, K. K., et al. 2015, Nature, 519, 327
Willott, C. J., Abraham, R. G., Albert, L., et al. 2017, CANUCS: The CAnadian NIRISS Unbiased Cluster Survey, JWST Proposal Cycle 1
Wyithe, J. S. B., & Loeb, A. 2005, ApJ, 625, 1
Yue, B., Castellano, M., Ferrara, A., et al. 2018, ApJ, 868, 115

Appendix A: Observed spectra

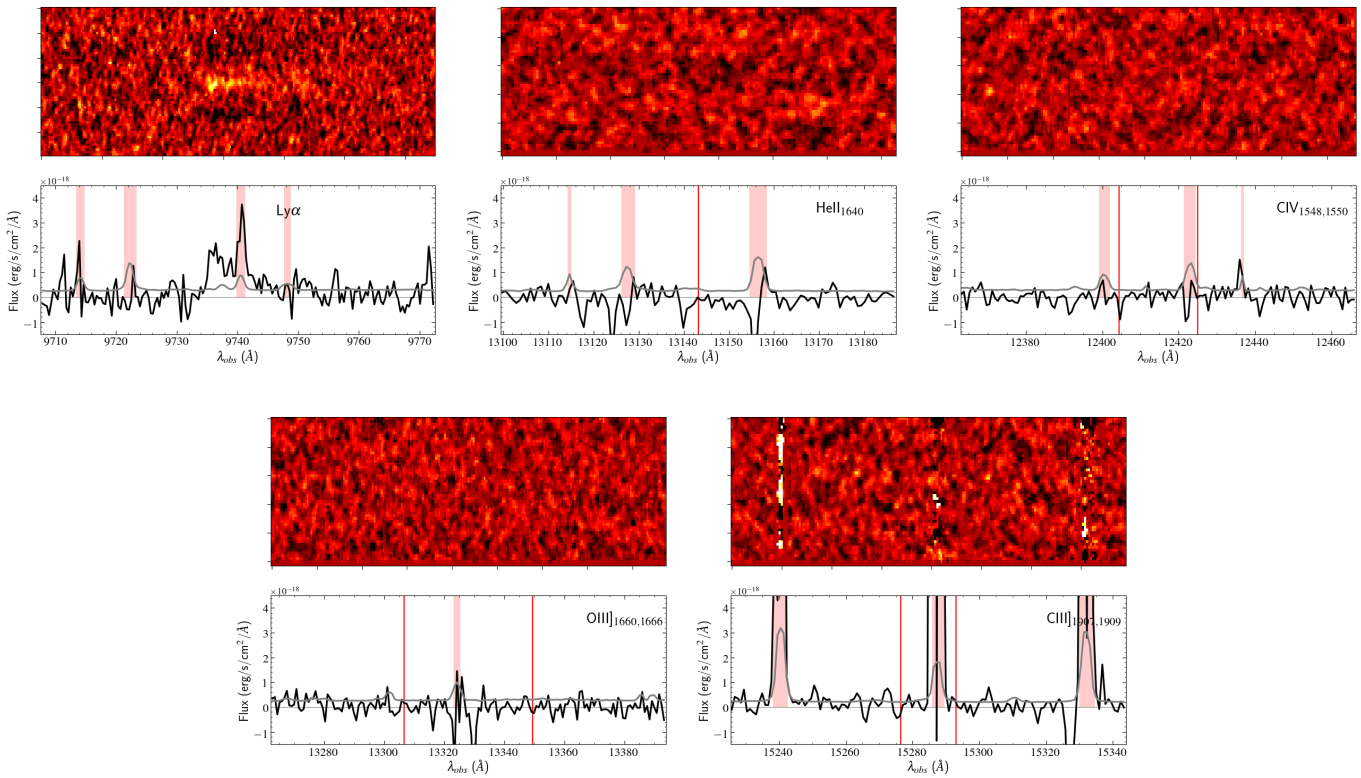

Fig. A.1. Observed spectral regions at the position of BDF521 UV lines observed by X-shooter. The regions cover the range from -1000 to +1000 km/s around the Lyα redshift. The red vertical lines mark the expected positions of UV lines or doublet components, assuming no velocity shift with respect to the Lyα redshift. The top panels show the 2D S/N spectrum, while the bottom panels show the 1D spectrum and rms as black and grey lines, respectively. The shaded red regions are masked due to contamination from sky lines.

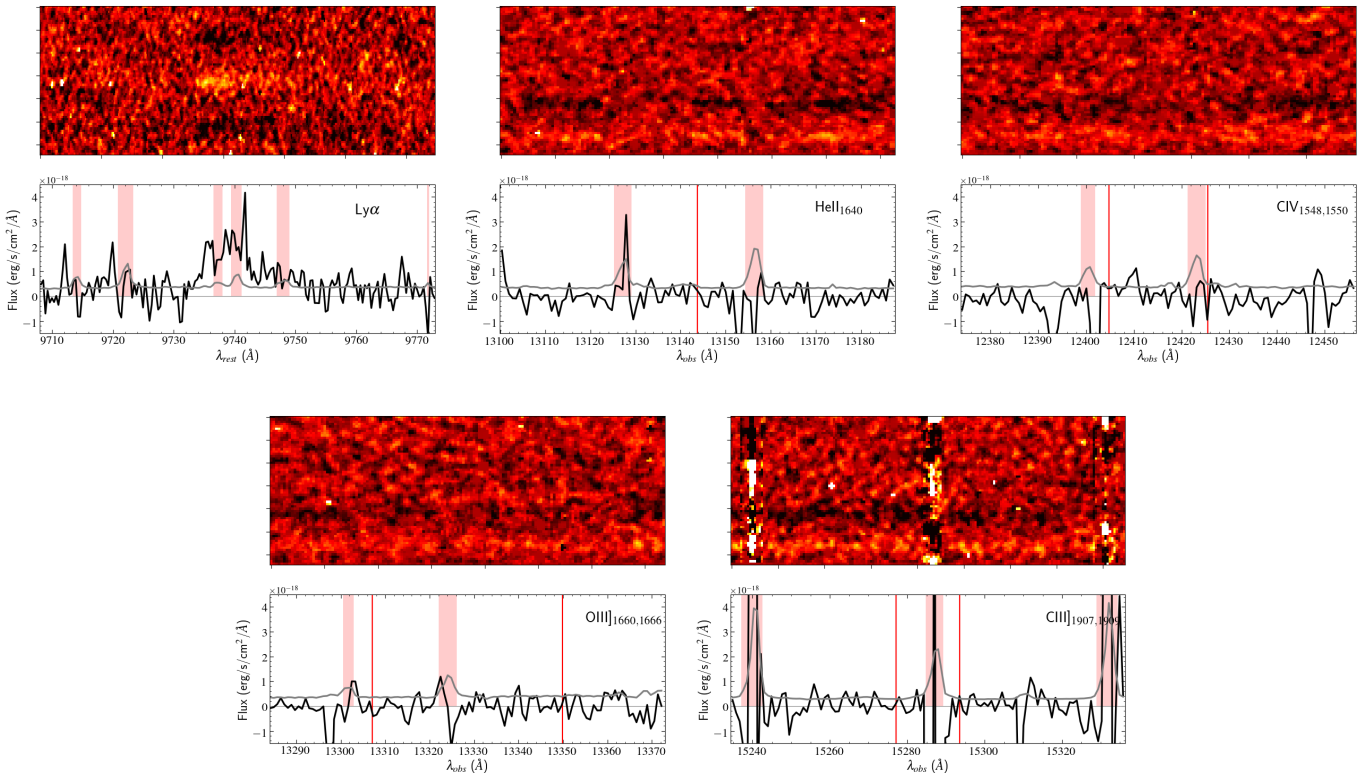

Fig. A.2. Same as A.1 but for BDF2195.